# Thermal detector based on a suspended polyimide membrane for infrared radiation applications

D. Bourgault,[1,2,a] G. Paul,[1,2] C. Latargez,[1,2] G. Moiroux,[1,2] D. Jegouso,[1,2] C. Felix,[1,2] C. Guttin,[1,2] and J.-L. Garden[1,2]

AFFILIATIONS

[1]University Grenoble Alpes, Institut Néel, F-38042 Grenoble, France
[2]Centre National de la Recherche Scientifique/Institut Néel, 25 Avenue des Martyrs, BP 166, 38042 Grenoble Cedex 9, France

**Note:** This paper is part of the APL Special Collection on Advances in Thermal Phonon Engineering and Thermal Management.
[a]Author to whom correspondence should be addressed: daniel.bourgault@neel.cnrs.fr

## ABSTRACT

This Letter details a pioneering study on the design and nanofabrication process of a thermoelectric infrared radiation detector using a suspended polyimide membrane. The research includes a comprehensive analysis of thermoelectric doped $Bi_2Te_3$ thin films, comparing their expected performance regarding noise and specific detectivity with other infrared detectors, particularly those in the silicon sector. Experimental results and calculations shed light on responsivity and time constants. In the absence of absorption layers, specific detectivity values for visible and near infrared radiation are measured at $9.2 \times 10^7$ and $2.9 \times 10^7$ cm $\sqrt{Hz}$/W, respectively, with a time constant nearing 20 ms. Calculations show that introducing an optimized absorption layer with $\varepsilon = 1$ significantly improves specific detectivity, reaching $9.0 \times 10^8$ cm $\sqrt{Hz}$/W. Subsequent calculations also show that further enhancement can be obtained by etching the polyimide membrane to a 1-micron thickness, resulting in an exceptional specific detectivity value of $8.4 \times 10^9$ cm $\sqrt{Hz}$/W, placing it among the best in the current state-of-the-art.

*Published under an exclusive license by AIP Publishing.* https://doi.org/10.1063/5.0213691

Infrared (IR) detectors have a wide range of applications, including night vision cameras, thermography devices, gas detectors, and various other equipment. They can be classified into two main types based on their method of detecting infrared radiation: quantum infrared detectors,[1,2] which directly absorb infrared rays using semiconductor materials, and thermal infrared detectors, which detect light by converting it into heat.[3–6]

The first type of detectors boasts exceptional sensitivity but typically requires a cooling mechanism to function optimally. In contrast, the second type of detector, while slightly less sensitive, offers a distinct advantage in its non-cooling design, making thermal infrared detectors particularly well suited for mobile devices.

Thermal infrared detectors can be further categorized into two subgroups: resistive bolometers[3] and thermoelectric infrared detectors, which are often called thermopiles.[4–6] Bolometers detect infrared radiation by measuring changes in the electrical resistivity of the materials used in the detector. They consume a minimal, continuous amount of electrical energy to induce these changes. On the other hand, thermopiles detect infrared energy without the need for external electrical power. However, they generally exhibit lower sensitivity compared to bolometers, emphasizing the need for significant sensitivity improvements in thermopile technology.

A material of the bismuth telluride type has already been used to develop IR thermopiles of good quality.[7–10] However, at that time, the development of this family of materials in thin films was not perfectly mastered, which limited thermoelectric (TE) performance. The figure of merit $ZT = S^2T/\rho\kappa$ ($\rho$ electrical resistivity, $\kappa$ thermal conductivity, S Seebeck coefficient, and T temperature) was not optimized with $ZT < 1$.

Currently, the most sensitive focal plane arrays (FPA) type thermopiles are made of doped poly-silicon[6] with a specific detectivity $D^* = \sqrt{A}\sqrt{B}/NEP$ (A absorbing surface, B frequency bandwidth, and NEP noise equivalent power defined mathematically in the supplementary material) higher than that of Ref. 10 or Ref. 11. Nevertheless, the intrinsic physical properties of doped poly-silicon will never result in a figure of merit equal to unity, like most of the TE-materials currently realizable and accessible.

In this study, we employed doped $Bi_2Te_3$ thin films optimized in previous research,[12,13] with a TE figure of merit ZT of 0.6 and 0.1 for n-type and p-type thin films, respectively. It is noteworthy that a

higher ZT corresponds to a lower noise equivalent power.[6,14] The key advantage of employing a material with ZT = 1 is the balance it strikes between Johnson and temperature noises (see simulations in the supplementary material). This equilibrium ensures that the detector is finely tuned for minimal noise. Our approach involves depositing TE-layers onto an ultra-thin, suspended polyimide membrane with low thickness (25 $\mu$m) and minimal thermal conductivity (0.2 W/m K). This design induces a potential substantial thermal gradient between the center and the periphery of the membrane[15] and is consequently very sensitive to IR radiations. We present the design and nanofabrication process of this innovative TE-detector, comparing its expected performance in terms of noise and specific detectivity with other IR detectors, particularly those within the silicon sector. Furthermore, we provide initial results regarding responsivity and time constants achieved in our experiments.

The performance of a TE device is connected to the figure of merit ZT,

$$ZT = \frac{S^2}{\rho\kappa}T \geq ZT_{eff} = \frac{S^2}{RK}T. \qquad (1)$$

The first equality applies to the TE-materials, while the second applies to the detector. The latter deals with the effective performance of the detector. It should be noticed that the equality is valid only for thermoelectric detector made of n-type and p-type materials with similar physical properties ($S_n = S_p$, $\rho_n = \rho_p$, and $\kappa_n = \kappa_p$). $R$ is the total resistance involving the resistivity $\rho$ of the TE-materials, but also the contact resistance between the different layers and also the resistances of the electrical connections (contact surfaces and contact wires). $S$ is the Seebeck coefficient, an intrinsic property that is highly dependent on the composition of the TE-materials. $K$ is the total thermal conductance, or thermal exchange coefficient, between the sensitive detector-area and the surroundings environment. It involves the thermal conductivity $\kappa$ of the TE-materials, but also all the other thermal links like TE-layers holder, gaseous loss, or spurious radiation links. A detector is perfectly optimized when $ZT_{eff} = ZT$. Since, in the better conditions, the $ZT$ of the Bi$_2$Te$_3$ deposited thin films is close to one, our principal task is to design a detector for which $ZT_{eff}$ tends to one. It is known that for $ZT_{eff} = 1$, the two principal sources of noise (Johnson noise and temperature noise) are equivalent[6,15] (see the supplementary material for NEP definition and simulation in this ideal case).

In the real detector configuration, there is a crucial limiting parameter, which is the thickness of the polyimide membrane that sustains the TE-thin films. Despite the low value of the thermal conductivity of such a polymeric material, the current membrane thickness is too high. The value of thickness ($e$) is 25 $\mu$m. The targeted value is of $e$ = 1 $\mu$m. The current thickness of 25 $\mu$m ensures a high robustness of the suspended membrane for the first experimental measurements presented in the following section. The expected thickness of 1 $\mu$m will be reached in a near future by classical plasma $O_2$ etching of the polyimide, once all the previous tests will be done [see the supplementary material for simulations of $\mathcal{R}_e$ [Fig. S2(a)], NEP [Fig. S2(b)], $\tau_{th}$ [Fig. S2(c)], and D* [Fig. S2(d)] as a function of thickness $e$]. Calculations show that by reducing the thickness of the polyimide membrane by a factor of 25, about one decade in performance may be obtained for the total NEP, $\mathcal{R}_e$, and D*, while the thermal relaxation time is reduced by a factor of only about 1.4 (see Fig. S2 in the supplementary material).

The substrate used is a polyimide membrane (Upilex®) of 25 $\mu$m thickness bounded on a copper ring (see Fig. 1) of 28 mm external diameter, with a 1 mm hole (D$_1$) in the center delimiting the sensitive area. The TE-thin films were deposited using a home-made dc magnetron sputtering chamber. 50 mm hot pressed targets were used with Bi$_2$Te$_{2.7}$Se$_{0.3}$ stoichiometric compositions for n-type and Bi$_{0.5}$Sb$_{1.5}$Te$_3$ for p-type materials. Pressure in the chamber before deposition is lower than $10^{-6}$ mbar, and then, the argon pressure is maintained around $1.5 \times 10^{-2}$ mbar during deposition. The plasma power is set to 10 W for a deposition time of 15 min (335 nm of thickness t). Each type of films is annealed in an oven under argon gas at atmospheric pressure during 2 h at 543 K before the deposition of a nickel/platinum layer for electrical contacts [Fig. 1(a)]. Such optimal annealing conditions were determined in previous studies for the crystallization of n-type and p-type Bi$_2$Te$_3$ films.[12,16]

Table I gives quantitative compositions of n-type and p-type films analyzed by energy dispersive spectroscopy performed with an environmental scanning electron microscope (ESEM FEI Quanta 200). Three different regions of each film were analyzed with the same conditions (accelerating voltage, beam current, magnification, and acquisition time). n-type and p-type films composition were, respectively, Bi$_{2.1}$Te$_{2.65}$Se$_{0.25 \pm 0.05}$ and Bi$_{0.55}$Sb$_{1.6}$Te$_{2.85 \pm 0.05}$.

Electrical contacts consist of a dual-layer structure comprising a 250 nm thick nickel layer and a 100 nm thick platinum layer. These layers are deposited both at the detector central region, within a 100 $\mu$m diameter circle (D$_2$), and along the periphery, covering a diameter ranging from 1 to 23 mm. The deposition process is realized through magnetron sputtering under an argon pressure of $10^{-2}$ mbar.

The detector, similar to any typical thermopile, consists of a sequence of TE-material, specifically n-type and p-type Bi$_2$Te$_3$ thin films in our particular configuration. Two distinct designs were formulated in this work, one featuring a single junction, and the other incorporating dual-junctions [see Figs. 1(b) and 1(c)]. Connecting multiple junctions electrically in series leads to a responsivity that is directly proportional to the number of junctions. However, since the surface covered by the TE layers is constant, the resistance is proportional to the square of the number of junctions. Consequently, the specific detectivity remains constant regardless of the number of junctions in series. The key benefit of increasing the number of junctions is that the impedance of the detector must be adapted to the impedance of the measuring equipment with equality of their Johnson noises.

TE properties are summarized in Table I. Seebeck coefficient ($S$) and electrical resistivity ($\rho$) have been measured with a home-made setup and four point method on films deposited on a substrate of 25 × 25 mm$^2$. The Seebeck coefficients for n-type and p-type TE-thin films are $-174$ and $+160$ $\mu$V/K, respectively, at room temperature. The electrical conductivities for these films are 2.8 and 9.75 m$\Omega$ cm. Referring to the thermal conductivity values provided in Table I and measured on thin films with similar compositions, the corresponding TE-figure of merit (ZT) values are found to be 0.6 for n-type and 0.1 for p-type TE-thin films. These values are lower than those obtained by Parashchuk et al. and Maksymuk et al.[17,18] These authors obtained figures of merit of 1 for n-type and p-type thin films. It should be noted that the detector developed in their study demonstrates a sensitivity of approximately 10 V/W, making it highly effective for detecting minimal heat flux levels as low as around $10^{-7}$ W.
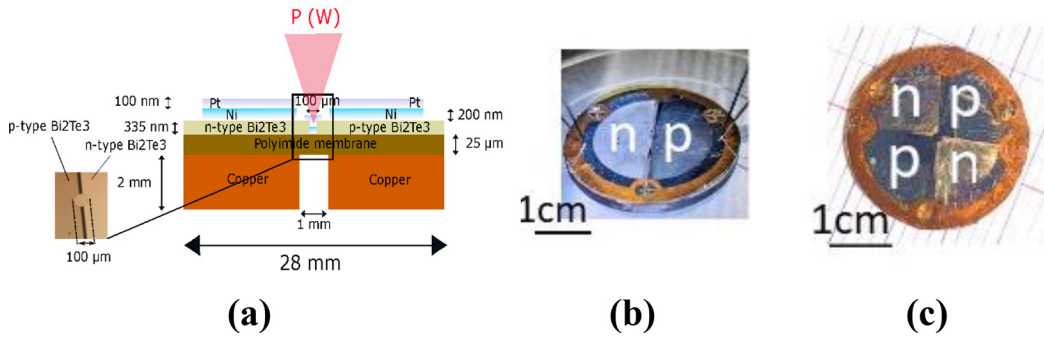
FIG. 1. Detector characteristics: principle of detector cross section (a) (scales are not respected) and optical pictures of $Bi_2Te_3$ detectors constituted of single (b) and dual-junctions (c).

The detector is fixed in a clamping ring, which is itself fixed to the 3D pallet. Copper wires are then connected to the contacts at the n–p junction terminals to measure the detector's internal resistance and the TE-voltage generated by the radiation.

An optical test bench allows to precisely focus a laser beam onto the 100-$\mu$m-wide active central region of the detector (see Fig. S3 in the supplementary material). This setup facilitates the evaluation of two essential performance criteria for the detector: responsivity ($\mathcal{R}_e = S/K$; see simulations in the supplementary material) and thermal relaxation time ($\tau_{th}$). The incident radiation creates a temperature difference between the center and the boundaries of the detector, which is then converted into voltage. This voltage is amplified, and the signal is captured either on a low noise voltmeter or an oscilloscope. In order to calibrate the incident power captured on the absorbing detector sensitive area, a photodiode is placed at the output of the objective to collect the power variation resulting from the change in the angle of the half-wave plate. For $\tau_{th}$ measurement, a chopper has been inserted in the optical bench between the half-wave plate and the objective. Two laser sources were used for the detector characterization: one in the visible part of the spectrum (671 nm) and a second one in the near-infrared (NIR) range (1064 nm).

Figure 2 illustrates the voltage generated in relation to the incident power of visible and NIR radiation for both single [Fig. 2(a)] and dual-junction [Fig. 2(b)] configurations. The corresponding responsivities ($\mathcal{R}_e$), determined from the slopes of the curves, are presented in

Table II. It is crucial to note that $\mathcal{R}_e$ is suboptimal (7.3 and 2.2 V/W for visible and IR radiation, respectively) when compared to the theoretical value calculated for a single junction (24 V/W, as indicated by the black crosses in simulations in the supplementary material). This suboptimal performance is attributed to the absence of a highly absorptive layer.

The choice of Pt to mitigate Ni oxidation proves to be less than ideal for absorbing infrared (IR) radiation. Research indicates that metals with high electrical conductivity exhibit low emissivity values, especially on polished deposition surfaces. Huang's study, for instance, measured values below 0.1 on polished Ni samples coated with a 500 nm layer of Pt within the 3–14 $\mu$m wavelength range.[19] Consequently, it is reasonable to assume that the emissivity of the Pt layer in our detectors hovers around 0.1 for NIR radiation. This observation is consistent with values derived from the ratio of theoretical and experimental responsivity, which stands at 2.4/2.2, approximating a ratio of 10. For radiation in the visible range, the ratio of theoretical and experimental responsivity, close to 4, is in agreement with the emissivity values obtained in the literature for Pt films.[20]

The responsivity of the detector constituted of dual-junctions is twice the value of single junction for visible as well as for IR radiation.

The time response $\tau$ is estimated from Fig. 3 showing the voltage generated by a radiation pulse at a frequency of 3 Hz. In the supplementary material, Fig. S4(a) shows an enlargement revealing the voltage increase during the pulse of NIR radiation, with a fitting curve following the law $A + B(1 - e^{-t/\tau})$. The voltage decrease after the radiation pulse [Fig. S4(b)] follows an exponential decay law. Experimental ($\tau$) and theoretical response times ($\tau_{th}$) for single and dual-junctions TE detectors exposed to visible and NIR radiation are summarized in Table II. The time constants are not dependent on the radiations and are close to the theoretical value $\tau_{th}$ calculated from C/K = 20 ms.

The resistances of the single and double junctions were measured and found to be 415 and 1409 $\Omega$, respectively. Calculated values based on electrical resistivity properties from Table I and geometry yielded 275 and 1100 $\Omega$, respectively. Discrepancies are attributed to contact resistance. Considering the surface area contributing to carrier injection (S = $7.85 \times 10^{-5}$ cm$^2$ at the central area), the contact resistivity is approximately 11 m$\Omega$ cm$^2$. This value exceeds those reported in the literature, typically in the range of a few $\mu$-$\Omega$ cm$^2$,[21,22] and necessitates improvement to reduce detector resistance.
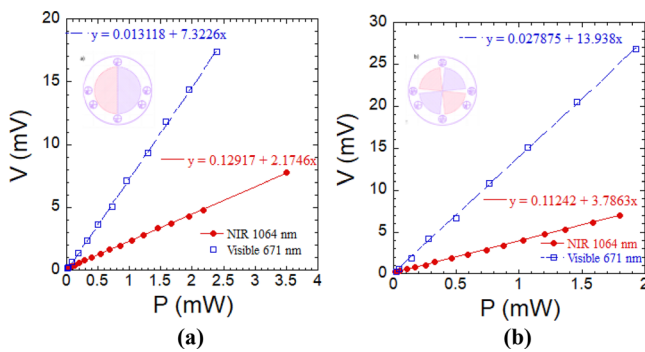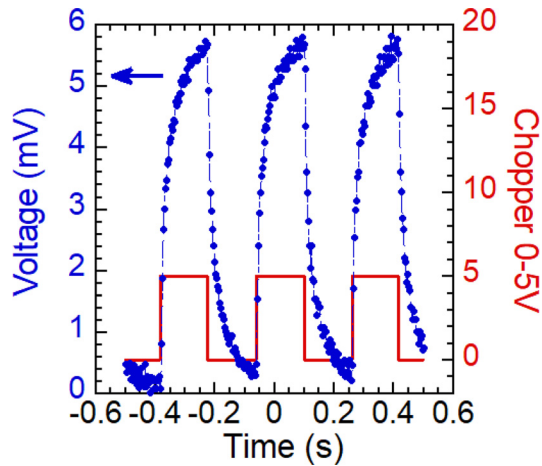


FIG. 2. Voltage generated vs laser's incident power for visible (blue empty square) and NIR radiation (red full disk) for single (a) and dual-junctions (b).

**TABLE I.** Thermoelectric properties of n- and p-type thin films. The thermal conductivity is taken from Ref. 12.

| | S ($\mu$V/K) | $\rho$ (m$\Omega$ cm) | $P_F$ power factor (mW/K$^2$ m) | $\kappa$ (W/mK) | ZT |
|---|---|---|---|---|---|
| n-type Bi$_2$Te$_{2.7}$Se$_{0.3}$ | −174 | 2.8 | 1.08 | 0.55 | 0.6 |
| p-type Bi$_{0.5}$Sb$_{1.5}$Te$_3$ | +160 | 9.75 | 0.26 | 0.79 | 0.1 |



**FIG. 3.** Voltage generated for dual-junctions plotted against time at a frequency of 3 Hz, with NIR radiation of 1.35 mW.

According to Eq. (S2) in the supplementary material, $NEP_{phon}$ obtained for single or dual-junctions is $8.5 \times 10^{-12}$ W/$\sqrt{\text{Hz}}$. The value is comparable to those found for Si TE detectors.[6] $NEP_{Joh}$ for single or dual-junctions is, respectively, of $3.59 \times 10^{-10}$ and $3.47 \times 10^{-10}$ W/$\sqrt{\text{Hz}}$ for visible radiation, respectively. These values increase to $1.19 \times 10^{-9}$ and $1.27 \times 10^{-9}$ W/$\sqrt{\text{Hz}}$ for NIR radiation. Significantly, these results deviate from the anticipated values outlined in simulations in the supplementary material, where a high figure of merit close to one was expected. The enhancement of transport electronic properties (S and $\rho$), coupled with the deposition of an efficient absorption layer, is anticipated to lead to a reduction in $NEP_{Joh}$.

$D^*$ values are summarized in Table III. The single couple gives a $D^*$ of $9.2 \times 10^7$ and $2.9 \times 10^7$ cm $\sqrt{\text{Hz}}$/W for, respectively, visible and NIR radiations.

These measurements are difficult to compare with values obtained for detectors measured in the LWIR, but given that emissivity

**TABLE III.** Specific detectivity D$^*$ for single and dual-junctions.

| | D$^*$ single junction (cm $\sqrt{\text{Hz}}$/W) | D$^*$ dual-junctions (cm $\sqrt{\text{Hz}}$/W) |
|---|---|---|
| Visible 671 nm | $9.2 \times 10^7$ | $9.0 \times 10^7$ |
| NIR 1064 nm | $2.9 \times 10^7$ | $2.3 \times 10^7$ |

in the visible and IR range is well below 1, the values obtained are very encouraging for operation in the LWIR. To this end, we estimated the responsivity and D$^*$ by assuming both a maximal emissivity of 1 and a realistic emissivity of 0.7, while also reducing the thickness of the polyimide membrane. The detailed calculations are provided in the supplementary materials, where the parameters K, C$_{tot}$, $\mathcal{R}_e$, NEP, $\tau$, and D$^*$ are plotted as a function of polyimide thickness. For these simulations, only the conductive thermal conductance associated with the polyimide and the thermoelectric layers was considered because of the low estimated values of the convective (K$_{conv}$) and radiative (K$_R$) thermal conductance quantities of $4.65 \times 10^{-8}$ and $4.8 \times 10^{-8}$ W/K, respectively (see the supplementary material).

For our detector with ZT$_n$ = 0.6 and ZT$_p$ = 0.1 and with an optimized absorption coefficient ($\varepsilon \sim 1$), we present expected values of $3.4 \times 10^8$ and $4.1 \times 10^9$ cm $\sqrt{\text{Hz}}$/W [refer to the supplementary material, Fig. S2(d) curves red] for polyimide thickness of 25 and 1 $\mu$m, respectively. For a realistic absorbing layer like TiN ($\varepsilon$ = 0.7), as used by A. Varpula et al.,[6] the calculated values are slightly reduced to $2.4 \times 10^8$ cm $\sqrt{\text{Hz}}$/W for a 25 $\mu$m thickness and $3.0 \times 10^9$ cm $\sqrt{\text{Hz}}$/W for a 1 $\mu$m thickness [see Fig. S2(d), blue curves]. These values are further compared to those obtained for state-of-the-art thermoelectric detectors in Fig. 4. These adjustments enhance the overall performance of our detectors, demonstrating their potential in the field of nano-TE-infrared detection.

It is important to note that, besides the polyimide etching and the addition of a highly absorbing layer, improvements in the electronic transport properties (S and $\rho$) of both n-type and p-type thin films are essential. In our current study, the figure of merit ZT is only 0.1 for the p-type and 0.6 for the n-type. Enhancing these values is crucial to approach the optimal value of 1, ensuring balanced Johnson and thermal noise. This enhancement will substantially decrease the noise equivalent power and improve specific detectivity (see Fig. S2 in the supplementary material). In Fig. 4, we have incorporated data points derived from simulated curves (refer to Fig. S2 of the supplementary material) corresponding to optimized n-type and p-type Bi$_2$Te$_3$ thin films with ZT = 1. These simulations yield expected values of $9.0 \times 10^8$ and $8.4 \times 10^9$ cm $\sqrt{\text{Hz}}$/W for polyimide thicknesses of 25 and 1 $\mu$m, respectively.

In conclusion, this study has presented the design and nanofabrication process of a groundbreaking innovative thermoelectric infrared

**TABLE II.** Experimental ($\mathcal{R}_e$ and $\tau$) and theoretical ($\mathcal{R}_{th}$ and $\tau_{th}$) responsivity and response time for single and dual-junctions TE detectors for visible and NIR radiation.

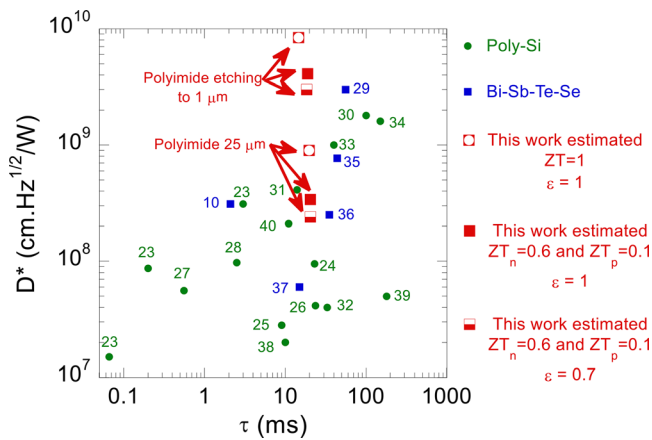| | $\mathcal{R}_e$ (and $\mathcal{R}_{th}$) single junction (V/W) | $\mathcal{R}_e$ (and $\mathcal{R}_{th}$) dual-junctions (V/W) | $\tau$ (and $\tau_{th}$) single junction (ms) | $\tau$ (and $\tau_{th}$) dual-junctions (ms) |
|---|---|---|---|---|
| Visible 671 nm | 7.3 (24 $\varepsilon$ = 1) | 13.9 (48 $\varepsilon$ = 1) | 18 (20) | 20 (20) |
| NIR 1064 nm | 2.2 (24 $\varepsilon$ = 1) | 3.8 (48 $\varepsilon$ = 1) | 17 (20) | 24 (20) |

**FIG. 4.** Time constants $\tau$ and specific detectivities $D^*$ of TE-bolometers developed with poly-Si[23–28,30–34,38–40] (green symbols) and Bi-Sb-Te-Se[10,29,35–37] (blue squares) thin films. Estimated specific detectivities on our detector with single junction have been added in the figure (red squares). The estimated values are calculated with $ZT_n = 0.6$ and $ZT_p = 0.1$ and for an absorption coefficient of $\varepsilon \sim 1$ (full square), with $ZT_n = 0.6$ and $ZT_p = 0.1$ and $\varepsilon = 0.7$ (semi-full square) and with $ZT = 1$ and of $\varepsilon = 1$ (empty square).

radiation detector utilizing a suspended polyimide membrane. The comparative analysis of thermoelectric doped $Bi_2Te_3$ thin films, evaluating their anticipated performance in terms of noise and specific detectivity against other IR detectors, particularly those in the silicon sector, has been elucidated. Our experimental findings have provided valuable insights into responsivity and time constants.

In the absence of absorption layers, the measured $D^*$ values for visible and NIR radiation stand at $9.2 \times 10^7$ and $2.9 \times 10^7$ cm $\sqrt{Hz}$/W, respectively, with a time constant approaching 20 ms. Calculations shown in the supplementary material indicate that the introduction of an optimized absorption layer with $\varepsilon = 1$ and the optimization of $Bi_2Te_3$ thermoelectric thin films to $ZT = 1$ result in a noteworthy improvement, yielding a $D^*$ value of $9.0 \times 10^8$ cm $\sqrt{Hz}$/W. Further enhancement can be achieved through polyimide membrane etching to a thickness of 1 $\mu$m, leading to a remarkable $D^*$ value of $8.4 \times 10^9$ cm $\sqrt{Hz}$/W, positioning it among the best values in the current state-of-the-art.

This work underscores the considerable potential of thermoelectric detectors, specifically those incorporating doped $Bi_2Te_3$ in conjunction with a suspended polyimide membrane, for infrared detection. The achieved performance metrics highlight the promising advancements and contributions of this innovative detector design to the field of IR sensing technology.

See the supplementary material for the phonon, Johnson, and photon noise equivalent power calculations, simulation of $\mathcal{R}_e$, NEP, $\tau_{th}$, and $D^*$ simulations as a function of the polyimide thickness, and optical test bench description.

## AUTHOR DECLARATIONS
### Conflict of Interest

The authors have no conflicts to disclose.

### Author Contributions

**Daniel Bourgault:** Conceptualization (equal); Funding acquisition (equal); Methodology (equal); Project administration (equal); Supervision (equal); Writing – original draft (equal). **Guillaume Paul:** Conceptualization (equal); Formal analysis (equal); Investigation (equal); Validation (equal). **Charlotte Latargez:** Conceptualization (equal); Formal analysis (equal); Investigation (equal); Methodology (equal); Validation (equal). **Gaël Moiroux:** Conceptualization (equal); Formal analysis (equal); Investigation (equal); Methodology (equal); Validation (equal). **David Jegouso:** Formal analysis (equal); Investigation (equal); Methodology (equal). **Corinne Felix:** Formal analysis (equal); Investigation (equal); Methodology (equal). **Christophe Guttin:** Formal analysis (equal); Investigation (equal); Methodology (equal). **Jean-Luc Garden:** Conceptualization (equal); Data curation (equal); Funding acquisition (equal); Project administration (equal); Supervision (equal); Writing – original draft (equal).

## DATA AVAILABILITY

The data that support the findings of this study are available from the corresponding author upon reasonable request.

## REFERENCES

[1]A. Rogalski and K. Chrzanowski, "Infrared devices and techniques," Opto-Electron. Rev. **10**(2), 111–136 (2002).

[2]A. Rogalski, "Infrared detectors: Status and trends," Prog. Quantum Electron. **27**, 59–210 (2003).

[3]P. Richards, "Bolometers for infrared and millimeter waves," J. Appl. Phys. **76**(1), 1–24 (1994).

[4]A. Graf, M. Arndt, M. Sauer, and N. Gerlach, "Review of micromachined thermopiles for infrared detection," Meas. Sci. Technol. **18**(7), R59–R75 (2007).

[5]A. Daniels, *Field Guide to Infrared Systems, Detectors, and FPAs*, SPIE Field Guides Vol. FG40, 3rd ed., edited by J. E. Greivenkamp (SPIE PRESS, 2018).

[6]A. Varpula, K. Tappura, J. Tiira, K. Grigoras, O. P. Kilpi, K. Sovanto, J. Ahopeito, and M. Prunnila, "Nano-thermoelectric infrared bolometers," APL Photonics **6**, 036111 (2021).

[7]M. C. Foote and E. W. Jones, "High performance micromachined thermopile linear arrays," Proc. SPIE **3379**, 192–197 (1998).

[8]M. C. Foote, E. W. Jones, and T. Caillat, "Uncooled thermopile infrared detector linear arrays with detectivity greater than $10^9$ cmHz$^{1/2}$ W," IEEE Trans. Electron Devices **45**(9), 1896–1902 (1998).

[9]M. C. Foote and S. Gaalema, "Progress toward high-performance thermopile imaging arrays," Proc. SPIE **4369**, 350–354 (2001).

[10]M. C. Foote, M. Kenyon, T. R. Krueger, T. A. McCann, R. Chacon, E. W. Jones, M. R. Dickie, J. T. Schofield, D. J. McCleese, S. Gaalema, and W. Hu, "Thermopile detector arrays for space science applications," in *Proceedings of International Thermal Detectors Workshop (TDW'03)* (NASA Center for AeroSpace Information, 2003), pp. 2-16–2-20.

18 November 2024 08:24:19

[11]D. Xue, W. Zhou, H. Zhang, Z. Ni, W. Li, J. Wang, and X. Li, "100-$\mu$m-scale high-detectivity infrared detector with thermopile/absorber double-deck structure formed in (111) silicon," IEEE Trans. Electron Devices **68**(12), 6233–6239 (2021).

[12]C. Giroud-Garampon, "Réalisation et étude des propriétés thermoélectriques de couches minces et nanofils de types $Bi_{2-X}Sb_xTe_3$ et $Bi_2Te_{3-x}Se_x$," Ph.D. thesis (Grenoble University, 2011).

[13]D. Bourgault, B. Schaechner, C. Giroud Garampon, T. Crozes, N. Caillault, and L. Carbone, "Transport properties of thermoelectric $Bi_{0.5}Sb_{1.5}Te_3$ and $Bi_2Te_{2.7}Se_{0.3}$ thin films," J. Alloys Compd. **598**, 79 (2014).

[14]U. Dillner, E. Kessler, and H.-G. Meyer, "Figures of merit of thermoelectric and bolometric thermal radiation sensors," J. Sens. Sens. Syst. **2**, 85–94 (2013).

[15]J.-L. Garden, C. Latargez, D. Bourgault, and G. Moiroux, "Détecteur thermique de rayonnement," demande de brevet n°2207983 (CNRS, 2022).

[16]D. Bourgault, C. G. Garampon, N. Caillault, L. Carbone, and J. A. Aymami, "Thermoelectric properties of n-type $Bi_2Te_{2.7}Se_{0.3}$ and p-type $Bi_{0.5}Sb_{1.5}Te_3$ thin films deposited by direct current magnetron sputtering," Thin Solid Films **516**, 8579–8583 (2008).

[17]T. Parashchuk, O. Kostyuk, L. Nykyruy, and Z. Dashevsky, "High thermoelectric performance of p-type $Bi_{0.5}Sb_{1.5}Te_3$ films on flexible substrate," J. Mater. Chem. Phys. **253**, 123427 (2020).

[18]M. Maksymuk, T. Parashchuk, B. Dzundza, L. Nykyruy, L. Chernyak, and Z. Dashevsky, "Development of the flexible film thermoelectric micro-converter based on $Bi_2Te_3$ alloys," J. Mater. Today Energy. **21**, 100753 (2021).

[19]Z. Huang, W. Zhou, and X. Tang, "Application of low-emissivity Pt layer on Ni alloy to high temperature," Acta Metall. Sin. **23**(1), 1–7 (2010).

[20]S. Deemyad and I. F. Silvera, "Temperature dependence of the emissivity of platinum in the IR," Rev Sci. Instrum. **79**, 086105 (2008).

[21]D. Tainoff, A. Proudhom, C. Tur, T. Crozes, S. Dufresnes, S. Dumont, D. Bourgault, and O. Bourgeois, "Network of thermoelectric nanogenerators for low power energy harvesting," Nano Energy **57**, 804–810 (2019).

[22]R. P. Gupta, R. McCarty, and J. Sharp, J. Electron. Mater. **43**, 1608–1612 (2014).

[23]A. Varpula, A. Murros, K. Sovanto, A. Rantala, D. Gomes Martins, K. Tappura, J. Tiira, and M. Prunnila, "High-performance silicon-based nano-thermoelectric bolometers for uncooled infrared sensing," Proc. SPIE **12737**, 1273702 (2023).

[24]M. Müller, W. Budde, R. Gottfried-Gottfried, A. Hübel, R. Jähne, and H. Kück, "A thermoelectric infrared radiation sensor with monolithically integrated amplifier stage and temperature sensor," Sens. Actuators A **54**, 601–605 (1996).

[25]Y. L. Li, H. Zhou, T. Li, Y. Wang, Y. Liu, and Y. Wang, "CMOS compatible 8 × 2 thermopile array," Sens. Actuators A **161**, 120–126 (2010).

[26]D. Xu, B. Xiong, Y. Wang, M. Liu, and T. Li, "Integrated micromachined thermopile IR detectors with an $XeF_2$ dry-etching process," J. Micromech. Microeng. **19**(12), 125003 (2009).

[27]W. Li, Z. Ni, J. Wang, and X. Li, "A front-side microfabricated tiny-size thermopile infrared detector with high sensitivity and fast response," IEEE Trans. Electron. Devices **66**(5), 2230–2237 (2019).

[28]W. Ke, Y. Wang, H. Zhou, T. Li, and Y. Wang, "Design, fabrication, and characterization of a high-performance CMOS-compatible thermopile infrared detector with self-test function," J. Micromech. Microeng. **28**, 125017 (2018).

[29]A. S. Gawarikar, R. P. Shea, and J. J. Talghader, "High detectivity uncooled thermal detectors with resonant cavity coupled absorption in the long-wave infrared," IEEE Trans. Electron Devices **60**, 2586–2591 (2013).

[30]F. Haenschke, E. Kessler, U. Dillner, A. Ihring, U. Schinkel, and H.-G. Meyer, "New high detectivity linear array for analytical measurement in the room temperature range," Proc. SPIE **8353**, 83531L (2012).

[31]C. Lei, H. Mao, Y. Yang, W. Ou, C. Xue, Z. Yao, A. Ming, W. Wang, L. Wang, J. Hu, and J. Xiong, "A double-end-beam based infrared device fabricated using CMOS-MEMS process," Sens. Rev. **36**, 240–248 (2016).

[32]T.-W. Shen, K.-C. Chang, C.-M. Sun, and W. Fang, "Performance enhance of CMOS-MEMS thermoelectric infrared sensor by using sensing material and structure design," J. Micromech. Microeng. **29**, 025007 (2019).

[33]M. Hirota, Y. Nakajima, M. Saito, and M. Uchiyama, "120 × 90 element thermoelectric infrared focal plane array with precisely patterned Au-black absorber," Sens. Actuators A **135**, 146–151 (2007).

[34]U. Dillner, E. Kessler, V. Baier, A. Berger, T. Eick, D. Behrendt, and H. Urban, "A 64-pixel linear thermopile array chip designed for vacuum environment," in *Proceedings of the 9th International Conference for Infrared Sensors and Systems*, Nuremberg, Germany, 30 May–1 June (Sensor + test, 2006), pp. 295–300.

[35]F. Volklein, A. Wiegand, and V. Baier, "High-sensitivity radiation thermopiles made of Bi-Sb-Te films," Sens. Actuators A **29**, 87–91 (1991).

[36]U. Dillner, V. Baier, E. Kessler, J. Müller, A. Berger, D. Behrendt, and H.-A. Preller, "A high sensitivity single-chip 4-element thermoelectric infrared sensor," in *Proceedings of the 8th International Conference for Infrared Sensors and Systems*, Nuremberg, Germany, 25–27 May (Sensor + test, 2004), pp. 149–153.

[37]G. R. Lahiji and K. D. Wise, "A batch-fabricated silicon thermopile infrared detector," IEEE Trans. Electron Devices **29**, 14–22 (1982).

[38]R. Lenggenhager, H. Baltes, and T. Elbel, "Thermoelectric infrared sensors in CMOS technology," Sens. Actuators A **37-38**, 216–220 (1993).

[39]P. M. Sarro, H. Yashiro, A. W. van Herwaarden, and S. Middelhoek, "An integrated thermal infrared sensing array," Sens. Actuators **14**, 191–201 (1988).

[40]Y. He, Y. Wang, and T. Li, "Simultaneously controlling heat conduction and infrared absorption with a textured dielectric film to enhance the performance of thermopiles," Microsyst. Nanoeng. **7**, 36 (2021).

18 November 2024 08:24:19